Journal of Materials Chemistry C

Plasmonic Mesoporous Gold-Based SERS-Microfluidic Platform for the Detection of Infectious Disease

Journal:	*Journal of Materials Chemistry C*
Manuscript ID	TC-ART-04-2024-001638.R2
Article Type:	Paper
Date Submitted by the Author:	13-Sep-2024
Complete List of Authors:	Masud, Mostafa Kamal; University of Queensland, Australian Institute for Bio-engineering and Nanotechnology (AIBN) ; Shahjalal University of Science and Technology School of Life Sciences, Biochemistry and Molecular Biology Natsuhara, Daigo; Toyohashi University of Technology, Department of Mechanical Engineering Dai, Yuchen; The University of Queensland, Australian Institute for Bioengineering and Nanotechnology Bashir, Javeria; The University of Queensland, Nugraha, Asep Sugih; The University of Queensland Alshehri, Saad; King Saud University, Chemistry Bando, Yoshio; King Saud University, Chemistry; University of Wollongong, Hossain, Md. Shahriar; University of Queensland, School of Mechanical and Mining Engineering Kaneti, Yusuf; The University of Queensland, Bioengineering and Nanotechnology Shibata, Takayuki; Toyohashi University of Technology, Department of Mechanical Engineering Yamauchi, Yusuke; University of Queensland, Chemical Engineering; The University of Queensland Australian Institute for Bioengineering and Nanotechnology,

Plasmonic Mesoporous Gold-Based SERS-Microfluidic Platform for the Detection of Infectious Diseases

Mostafa Kamal Masud,[a] Daigo Natsuhara,*[b] Yuchen Dai,[a] Javeria Bashir,[a] Asep Sugih Nugraha,[a] Saad M. Alshehri,[c] Yoshio Bando,[c,d] Md Shahriar Hossain,[a,e] Yusuf Valentino Kaneti,[a] Takayuki Shibata,*[f] Yusuke Yamauchi*[a,b,g]

[a]*Australian Institute for Bioengineering and Nanotechnology (AIBN), The University of Queensland, St. Lucia, QLD 4072, Australia*

[b]*Department of Materials Process Engineering Graduate School of Engineering, Nagoya University, Nagoya, 464-8603, Japan*

[c]*Department of Chemistry, College of Science, King Saud University, Riyadh 11451, Saudi Arabia*

[d]*Australian Institute for Innovative Materials, University of Wollongong, North Wollongong, New South Wales, Australia*

[e]*School of Mechanical and Mining Engineering, Faculty of Engineering, Architecture, and Information Technology (EAIT), The University of Queensland, St Lucia, QLD, 4072, Australia*

[f]*Department of Mechanical Engineering, Toyohashi University of Technology, Aichi 441-8580, Japan.*

[g]*Department of Chemical and Biomolecular Engineering, Yonsei University, 50 Yonseiro, Seodaemun-gu, Seoul, 03722, Republic of Korea.*

Corresponding authors' emails: d-natsuhara@mems.me.tut.ac.jp (DN); shibata@me.tut.ac.jp (TS); y.yamauchi@uq.edu.au (YY)

Abstract

Infectious diseases, particularly those caused by pathogens and parasites, present significant global health challenges. Despite advancements in medicine, these diseases continue to result in high rates of illness, loss of function, and mortality. The continuous COVID-19 pandemic, stemming from the severe acute respiratory syndrome coronavirus 2 (SARS-CoV-2), highlights the critical necessity for early detection strategies to improve patient outcomes. We present a novel microfluidics platform for the simultaneous detection of proteins (antigens) crucial for SARS-CoV-2 identification: S1, RBD, and NCD. By combining microfluidics with Surface-enhanced Raman scattering (SERS), the platform enables highly sensitive and multiplexed detection of viral proteins. Furthermore, it employs an engineered mesoporous gold nanoparticles (mAuNPs)-based SERS nanotags to achieve a highly sensitive readout. Demonstrating excellent analytical performance, our platform simultaneously detects three antigens, achieving detection levels as low as 14 pg/mL, with an RSD of <5.0% (n = 3). Compared to existing approaches, our platform offers critical improvements for SARS-CoV-2-like infectious disease analysis. It provides a multiplex detection system alongside controls, a simple experimental setup, and a single-device-based complete assay platform. The mAuNPs-based SERS nanotags s eliminate the need for enzymatic amplification, while the portable SERS readout facilitates an in-field detection without sophisticated instrumentation or laboratory requirements.

Keywords: Microfluidics; SERS; SARS-CoV-2; mesoporous gold; infectious diseases.

Introduction

Infectious diseases pose significant challenges to global health, demanding a thorough grasp, preventative actions, and efficient treatment approaches. Throughout history, the pathogens and parasites responsible for these diseases have remained among the deadliest threats to humanity, with high rates of illness, impairment, and mortality persisting to this day (WHO, 2015).[1, 2] For instance, severe acute respiratory syndrome coronavirus 2 (SARS-CoV-2), which is the seventh known coronavirus, has caused a worldwide spreading pandemic since 2019. There have been 772,166,517 confirmed cases of COVID-19, including 6,981,263 deaths, reported to WHO.[3] Given the close relationship between disease severity and prognosis, adhering to basic and essential strategies is crucial for improving treatment outcomes. Among these strategies, early detection of high-risk and critically ill patients stands as paramount.[4] Hence, the early detection of SARS-CoV-2 as well as any virus is of great importance to reduce the mortality and relative burdens of any infectious disease.

To date, the most widely used two methods for detecting SARS-CoV-2 are the real-time reverse transcription-polymerase chain reaction (RT-PCR) and the rapid antigen test (RAT). It is believed that the RT-PCR is more accurate, especially when detecting small amounts of the virus, but much more time-consuming (around 24 hours), while the RATs can provide a rapid result (within 15 minutes) but with lower reliability.[5] Nevertheless, due to the limited testing of only one protein (single biomarker) and the lower sensitivity and specificity of RATs compared to qPCR, false negatives are frequently encountered.[6] Variations in RAT sensitivity are prevalent among different manufacturers, with an approximate sensitivity rate of 91%, which proves insufficient in a pandemic scenario where comprehending the activity of SARS-CoV-2 relies heavily on contact tracing and accurate infection rate assessment.[7] Furthermore, while RT-PCR proves valuable for the initial diagnosis, antigen tests (protein) like Ag-RDTs can effectively signal the conclusion of the isolation period. This is attributed to the fact that viral RNA, detectable by RT-PCR, may persist even in the absence of an infectious virus. In contrast, the positivity of antigen test typically indicates the presence

of an infectious virus.[8] The expression of the detected antigen(s) occurs only when the virus is actively replicating. Consequently, these tests cannot be utilized to identify acute or early infections.

Understanding the molecular characteristics of the virus is instrumental for developing dependable assays for detecting viral genomic RNA and proteins. SARS-CoV-2 encompasses four structural proteins and sixteen non-structural proteins (NSPs).[9] The structural proteins, namely nucleocapsid (N), envelope glycoprotein spike (S), envelope (E), and transmembrane (M), form the envelope and the capsid.[10, 11] The nonstructural proteins encoded by ORF1ab, such as RNA-dependent RNA polymerase (RdRp) and helicase (Hel), primarily facilitate viral replication. Quantitative RT-PCR assays are the mainstay of molecular COVID-19 diagnoses worldwide. Various PCR assays target several conserved regions in the SARS-CoV-2 genome, chosen as reliable primer design targets. In clinical settings, the WHO recommends using at least two targets to mitigate the risk of potential genetic mutations of SARS-CoV-2 or cross-reactions with other coronaviruses.[12] Compared to traditional sequencing methods or single-protein detection, which are often costly or prone to false positives, newly emerging portable methods offer cost-effective and high-throughput diagnoses by detecting multiple proteins simultaneously. These advancements hold promise for achieving accurate diagnosis, particularly during pandemic.

Microfluidics refers to systems that manipulate and analyze small volumes of fluids, integrating tools to control chemical, biological, and physical processes. This technology has evolved over time, with microfluidics and nanotechnology now playing crucial roles in developing diagnostic tools. Recent advancements in microfluidic technology have emerged as a potent force in enhancing personalized disease diagnosis and treatment methods.[13, 14] In comparison to conventional approaches, microfluidic devices require significantly smaller volumes of biological samples to detect the disease biomarkers swiftly. Additionally, the utilization of a multichannel detection technique allows for parallel assay analysis on a single microfluidic device, yielding statistically significant data for analysis.[15] Furthermore, employing microfluidic devices in creating individualized care plans enables

precise and rapid control over drug delivery profiles. This customization entails tailoring the methods of drug administration for each patient, ensuring accurate and timely treatment.

Surface-enhanced Raman scattering (SERS) stands out as a remarkably sensitive spectroscopic technique capable of detecting molecules at the single-molecule level.[16] By employing plasmonic nanostructures to enhance Raman signals and conjugating bioprobes like antibodies to create barcodes, SERS enables the multiplexed detection of various targets.[17] SERS-based bioassays predominantly rely on plasmonic noble metal nanostructures, such as gold (Au) or silver (Ag).[18] The superior plasmonic properties, chemical stability, biocompatibility, ease of functionalization, and versatility of Au make it an ideal material over others for a wide range of applications, particularly in the field of biosensing.[19-22] The various shapes and surface properties of Au result in distinct distributions and amplitudes of the electromagnetic field, while size-dependent plasmonic properties and nanostructure arrangements generate hotspots, leading to amplified Raman signals. A previous research has demonstrated that the combination of Au, Ag, and copper (Cu) within a single particle in trimetallic compounds significantly enhanced the SERS response.[23, 24] However, the integration of multiple NPs into a single material poses challenges, requiring intricate chemistry and being prone to inconsistencies. Hence, there is a growing demand for engineering a single metal-based particle with an exceptional SERS signal enhancement capability. In this context, the use of mesoporous gold nanoparticles (mAuNPs) for preparing SERS nanotags is proven to be highly advantageous. The precisely engineered exterior surface and interior voids of mAuNPs provide expansive surfaces and spacious cavities, facilitating the acquisition of distinctive physicochemical properties and maximizing material utilization efficiency. The abundance of Au surface and high-index facets further enhances the activity and selectivity of mAuNPs in enhancing SERS signals.[25] Additionally, the pores within mAuNPs establish electromagnetic (EM) boundary conditions (the electric and magnetic fields values at the interface between the pore wall), fostering the creation of intense and intricately structured EM fields through surface plasmon resonances. Thus, mAuNPs may play a pivotal role in amplifying SERS signals, enabling the ultra-sensitive detection of disease-specific

molecules. Therefore, the integration of mAuNPs-based SERS assay with a microfluidic device offers reliable, accurate, and multiplex detection of viral pathogens, including SARS-CoV-2 and other viruses.

In this work, we present an integrated microfluidic system designed for the rapid detection of SARS-CoV-2 by analyzing three associated proteins: nucleocapsid (N), envelope glycoprotein spike (S), and envelope (E). To achieve a highly sensitive detection, we employed an engineered mAuNPs-based SERS tag. Additionally, a five-chamber microfluidic system was utilized for simultaneous analysis of the three proteins and two controls. Our microfluidic platform allows for the analysis of three proteins and two controls in a single run, requiring only a minimal sample volume (~100 μL). Demonstrating excellent analytical performance, our platform can detect proteins at concentrations as low as 14 pg/mL, with a relative standard deviation (RSD) of <5.0% (n = 3). The platform is rapid, sensitive, and semi-automated, thus showing a high potential for translation into clinical settings for real-world applications.

Results and discussion

Assay Principle for mAuNPs-SERS microfluidic platform. This study introduces a rapid and straightforward SERS-based platform for the simultaneous detection of three SARS-COV-2 associated proteins named nucleocapsid (N), envelope glycoprotein spike (S), envelope (E) proteins in a single run. **Figure 1** demonstrates the SERS microfluidic platform for multiplex detection of these proteins. Two key innovations enable this simultaneous and sensitive detection: the microfluidic design, which allows easy and single-run detection of the three proteins, and the mAuNPs-based SERS nanotags, which ensures sensitive detection. The platform utilizes a three-chamber setup, each chamber forming a sandwich assay, alongside two control chambers. Specific antibodies are immobilized on the glass surface of each chamber using EDC-NHS chemistry to capture the respective SARS-CoV-2 proteins. For instance, a biotinylated RBD antibody is immobilized in the chamber designated for RBD protein detection, where the anti-RBD antibody binds to the RBD present on the surface of the spike protein.[26,27] To prevent the non-specific attachment or signal, each chamber is incubated with 0.5% BSA for 30 minutes followed by washing with binding and washing (b&w) buffer. After washing, the mAuNPs-based SERS tag is introduced into the chambers to recognize the proteins *via* IgG-protein interactions. The mAuNPs-based SERS nanotags consisting of mAuNPs, 4mercaptobenzoic acid (4-MBA) reporter, and IgG antibody, is prepared by forming a thiol monolayer with dithiobis (DSP, succinimidyl propionate) and a specific Raman reporter (4-MBA). After conjugating a secondary antibody specific to the target protein, the mixture was incubated, centrifuged, and resuspended multiple times. The final colloid, stabilized with bovine serum albumin (BSA) to reduce aggregation and non-specific binding, was used for immunoassay formation and SERS detection. Finally, a portable Raman spectrophotometer reads the nanotags presence in each chamber. The amount of nanotags present in each chamber is related to the amount of target proteins present in each chamber. The use of mAuNPs is crucial as it provides a larger surface area for loading a higher amount of the Raman reporter and provides more space for antibodies (see Experimental Section for details). For analysis, we identify the characteristic Raman

peak of 4-MBA at around 1588 cm^{-1}. The corresponding peak from each chamber represents the amount of protein present, allowing for simultaneous screening and quantification of the three proteins from the three chambers.

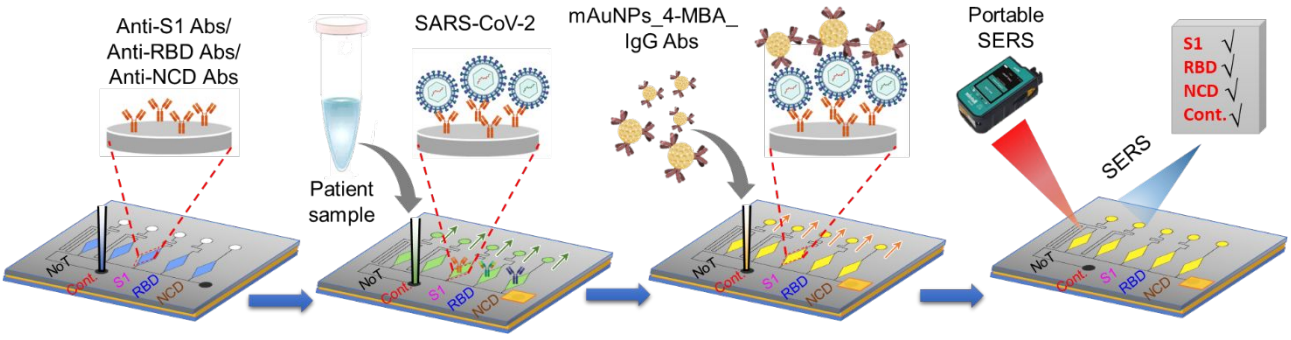

Figure 1. Workflow of the SERS microfluidic platform for multiplex detection of SARS-CoV-2 proteins. The PDMS device is placed on glass followed by the modification of each chamber with respective antibodies. The sample is then passed through the device where the spike proteins attach with the respective antibody. The SERS nanotags with IgG antibodies are passed through the chamber for assay formation (target-specific recognition. Finally, a portable SERS readout records the spectra from each chamber with respect to two controls.

Working principle of microfluidic device. The working mechanism of the microfluidic device (array sensor) is illustrated in **Figure 2**, demonstrating the manipulation of liquid for SERS detection. The polydimethylsiloxane (PDMS)-based microfluidic device was fabricated following our previous report.[28] The device consists of five assay chambers, with three designated for different target proteins, and two for assay control and system control, respectively. The five microchambers are connected *via* two separate rectangular microchannels (with dimensions of 200 µm in width and 50 µm in height) (**Figure S1** and **Figure S2**). These microchannels serve to introduce liquid into the microchambers and expel air from them. The diluted sample is then introduced into the device through an inlet port using an electric pipette (250 µL pipette; Icomes Lab, Iwate, Japan). Initially, we demonstrate the

device's performance using two different coloured dyes to illustrate the efficiency and mechanism of sample loading, device control, and washing steps, as the assay involves multi-step processes: antibody loading, washing, sample loading, reporter binding, and finally, SERS reading steps. For the first step of sample loading, the flow of liquid (blue-coloured water) stops after reaching valve S_1 (P_1 = 1.87 kPa) and is redirected toward the microchamber. Once the microchamber is filled, the liquid flow stops at valve S_2 (P_2 = 4.97 kPa). The liquid then flows towards the second microchamber by passing through valve S1 because $P_1 < P_2$. By repeating these processes, all microchambers can be sequentially filled with liquid within 2 minutes. For the second step of the washing process, a common outlet port is sealed with a double-sided tape. Subsequently, a red-coloured water was introduced into the device from the same inlet port. As a result, the blue-coloured water was washed away from the microchambers by passing through valve S_2 and was simultaneously replaced by the red-coloured water in all microchambers within 2 minutes. The working principle of the microfluidic device is visually demonstrated in **Video S1** and **Video S2**. The two steps are repeated for subsequent procedures to complete the assay.

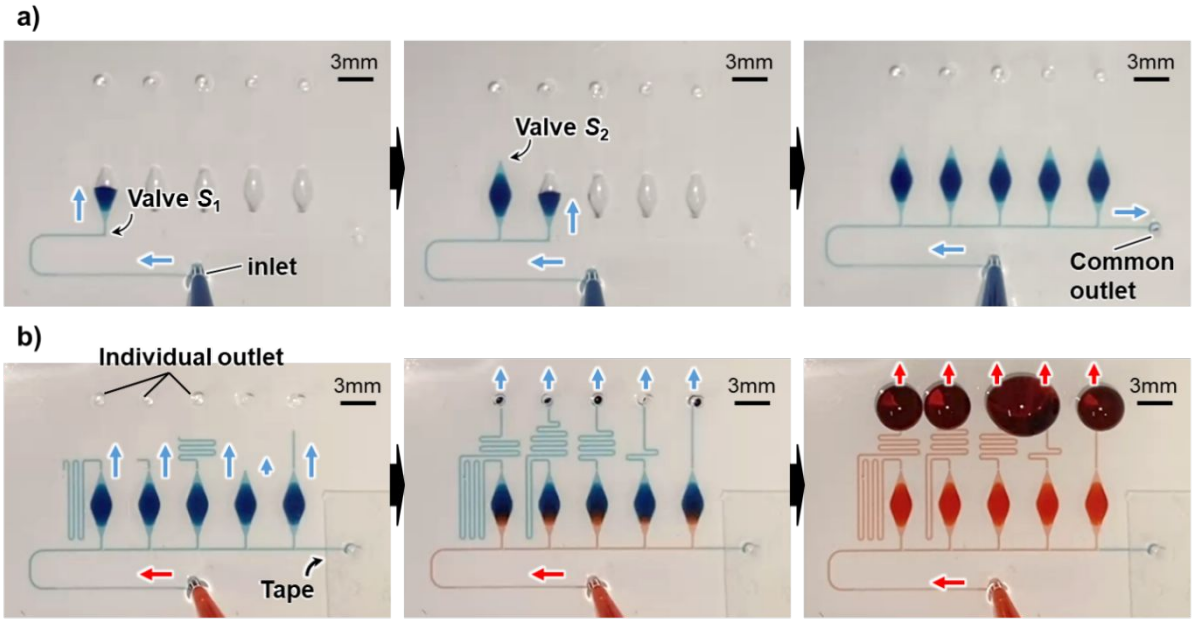

Figure 2. Experimental results showing the liquid manipulation in the microfluidic device. a) Sequentially dispensing of blue-coloured water into five microchambers. b) Washing away the blue-

coloured water and simultaneously replacing it with red-coloured water in all the microchamber at a constant flow rate.

SERS performance of mesoporous gold. Roughened Au surfaces with nanoscale features can enhance the SERS signal.[29] The rough surface of mAuNPs create numerous local electromagnetic hotspots due to plasmonic effects, resulting in a higher enhancement of the Raman signal.[30] The increased surface area and electromagnetic field enhancement also contribute to the overall improvement in SERS signal. In this assay design, mAuNPs are synthesized by using a soft-templating strategy following our previous report.[31] The scanning electron microscopy (SEM) images in **Figure 3a** reveal that the pores are distributed both internally and externally within the AuNPs. Furthermore, it can be observed that the mAuNPs are well-dispersed with highly uniform shape and size. The average diameter of this sample is 197.8 ± 5 nm. SEM imaging further unveiled that the surfaces of these NPs are adorned with numerous pores with an average pore size of 18.3 ± 2 nm, and pore walls with an average thickness of 17.3 ± 2 nm (**Figure S3**). To investigate the plasmon modes of the synthesized mAuNPs, UV-Vis spectroscopy was performed. As shown in **Figure S4**, the mAuNPs display a redshift compared to their non-porous counterparts, which is consistent with our previous study.[31] This redshift suggests that the porosity facilitates the penetration of multipolar plasmon resonances deep into the internal pores, where the lower effective dielectric constant results in a shift to longer wavelengths. Additionally, the porous structure creates nanoscale junctions within the nanoparticles, which contribute to the redshift of the plasmon modes without altering the overall size of the nanoparticles. Furthermore, the large pores induce symmetry breaking by interacting with time-dependent electric fields. This interaction enhances local electric fields due to asymmetric charge distributions in hybridized plasmon modes, resulting in hotspots both on the outer surfaces and within the pores of the mAuNPs. As a result, the plasmonic effects are extended to both exterior and interior regions, enhancing the overall electric field and improving surface utilization. Additionally, the large pores facilitate further symmetry breaking, leading to the overlap of

quadrupolar and dipolar modes and the formation of strongly hybridized plasmon modes.[31] These unique characteristics structure, which facilitate the high distribution of hotspots, make mAuNPs a superior candidate for SERS-based applications. The SERS activity of mAuNPs was compared with non-porous AuNPs of similar size. Both freshly prepared mAuNPs and non-porous AuNPs were tagged with 4-MBA, and SERS spectra were obtained to identify the distinctive peaks of 4-MBA. The mAuNPs display a two-fold signal enhancement compared to non-porous AuNPs, which is attributed to the presence of hotspots resulting from their mesoporous structure (**Figure 3b**). In mAuNPs, large electromagnetic fields arise around individual mesopores due to the charge induced at the surface of the pores from the extensive Au volume exposed to the electric field of incoming light.[32] Furthermore, the large pores respond more efficiently to light because their sizes approximate the wavelength of the oscillating charge density waves on the Au surface induced by visible light. Though the enhancement is two-fold, the mesoporous system plays multiple roles; not only for enhancing the SERS signal but also for loading of a large number of antibodies (IgG), which substantially enhances the sensitivity of biosensing. To establish the optimum saturation point for mAuNPs with Raman reporter (4-MBA), a series of samples with varying concentrations of 4-MBA were subjected to SERS analysis (**Figure S5**). The results of this analysis show the combination of 1 mL of mAuNPs with 200 μL of 4-MBA, in a ratio of 4:1, yield the highest signal intensity. Therefore, this ratio was chosen and used for subsequent experiments. It is important to check the SERS nanotags dispersibility and stability over time as well-dispersed SERS reporters are essential for obtaining reproducible, accurate and consistent SERS signal. The SERS measurements of the nanotags were performed over 14 days. It is found that the reporters can remain well-dispersed and maintain the SERS response (RSD<9%) over the 2 weeks, thus reflecting the high dispersibility of our nanotags (**Figure S6**).

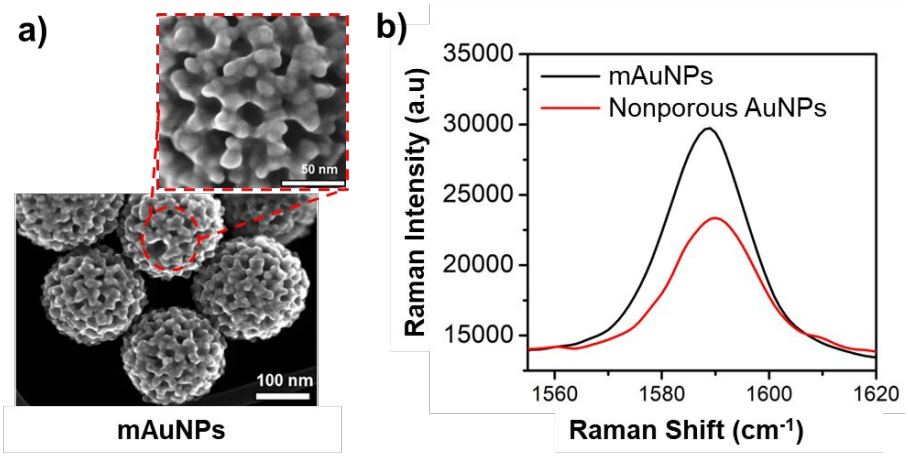

Figure 3. a) SEM image of mAuNPs synthesized with $PS_{18,000}$-*b*-PEO_{7500} block copolymer. b) Raman spectra of mAuNPs and non-porous AuNPs labelled with 4-MBA, measured at a wavelength of 785 nm.

Microfluidic assay specificity for S1, RBD and NCD. To assess the specificity and functionality of our simultaneous detection platform, we have conducted a series of control experiments. In positive control experiments, we functionalized chambers 3 to 5 with biotinylated anti-S1, RBD, and NCD antibodies, respectively, to capture the specific surface proteins of SARS-CoV-2 followed by recognition using the mAuNPs-based SERS nanotags functionalized with IgG. The sandwich assay (**Figure 1**) brings the mAuNPs-based nanotags which ultimately generate the SERS response. In the assay, the mAuNPs are randomly interconnected with each other (**Figure S7**). The high SERS response of mAuNPs arises from hotspots generated by both individual and interconnecting mAuNPs as shown by the mapping image of positive control (**Figure S8**). As shown in **Figure 4**, three chambers show clear intense peaks near wavelengths of 1585 to 1587 cm^{-1} corresponding to 4-MBA. As 4-MBA attached in SERS nanotags with IgG binds with the protein, the obtained peaks represent the corresponding amount of proteins. For the same amount of input (10 ng/mL), RBD has the highest intensity (1134), whereas NCD and S1 show relatively less (689 and 665, respectively) (**Figure 4**). Along the three target proteins, chambers 1 and 2 were designated for controls. The first chamber serves as a no-template control (NoT), where PBS is used instead of capture antibody. The second

chamber acts as another control, where the SERS reporter is replaced with PBS. The SERS spectra were recorded for both two chamber and it has been showed that, there is no signal specific to 4-MBA region. Without IgG, no SERS-CoV-2 was attached on the chamber, hence no sandwich assay formation with the protein as well as SERS nanotags, hence no signal. On the other hand, when we replaced the SERS nanotags with PBS, there was no signal in the region, *i.e.*, no background signal from platform surface or proteins. These control experiment indicates the platform enable to generate SERS signals respective to proteins whereas in the same run controls are not generating any corresponding signals, signifying the high specificity of the platform.

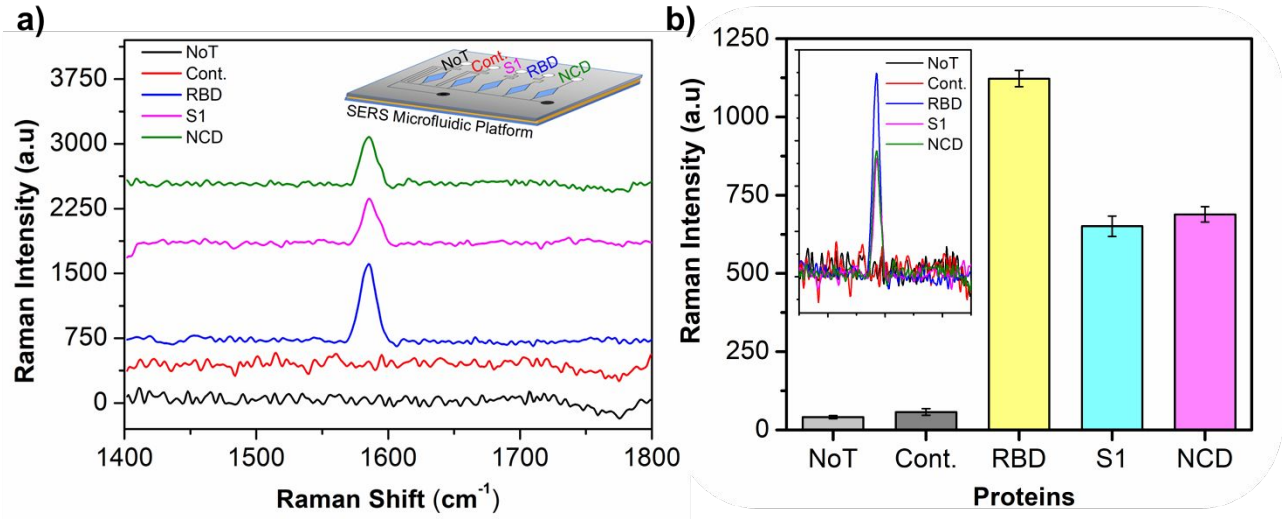

Figure 4. Assay specificity of the microfluidic platform. a) SERS spectra of three proteins S1, RBD and NCD along with two controls (NoT, where no capture antibody was used and Cont. where no SERS nanotags is used. *inset*; the platform with identified chambers) and b) corresponding bar diagram (i*nset*: merged spectra obtained using the microfluidic platform).

Sensitivity of the microfluidic platform. To assess the sensitivity of the microfluidic platform, we conducted tests to ensure its capability to detect minimal levels of SARS-CoV-2, which is crucial for detecting early phases of infection, often preceding the manifestation of symptoms. Given their non-specific clinical presentation, the accurate identification of SARS-CoV-2 infections relies heavily on

specific and sensitive diagnostic tools.[33] Expressed antigen(s) can normally be detected when the virus is actively replicating. Therefore, these tests can be utilized to identify acute or early infections. However, the expression of proteins at the beginning of replication is less, therefore detecting a trace amount of antigens or proteins to identify SARS-CoV-2 before an individual shows symptoms is crucial to minimize viral transmission. To determine the sensitivity of our assay platform, a designated concentration of S1 proteins spiked in PBS was prepared by serial dilution and quantified using the microfluidic system. As depicted in **Figure 5**a, b, the SERS response increases gradually with increasing concentration of S1 proteins. This is because more S1 proteins present in the sandwich assay can bind to SERS reporter nanotags, which lead to the increased SERS signal. The increment with the increase of S1 concentration follows a linear trend (Figure 5c) and the linear regression equation is found to be $y = 216.52x + 25.82$, with a correlation coefficient (R^2) of 0.9345. Very similar responses were also obtained for RBD and NCD proteins (**Figure S8**). The relative standard deviation (% RSD) of three independent measurements is <5.0%, suggesting the good reproducibility of our platform. The LOD was calculated by considering a signal-to-noise 3 ($s/n = 3$) and it is estimated to be 14 pg/mL, which is highly comparable to or lower than most of the reported assays (**Table S1**).[34-43] The nucleocapsid (N) protein can be detected at levels ranging from a few picograms (pg) to several nanograms (ng) per millilitre in various sample types for diagnosis purposes, which are possible by this platform, representing translational potentiality. While other reported sensors demonstrated an LOD of ng/mL, this report achieves a pg/mL level of detection in a multiplexed format inside of a device.[44] For instance, a multiplexed SERS micro assay was reported for detection of SARS-CoV-2, in which LOD was reported to be 50 pg/mL.[45] However, the design and fabrication are more complex than our platform.

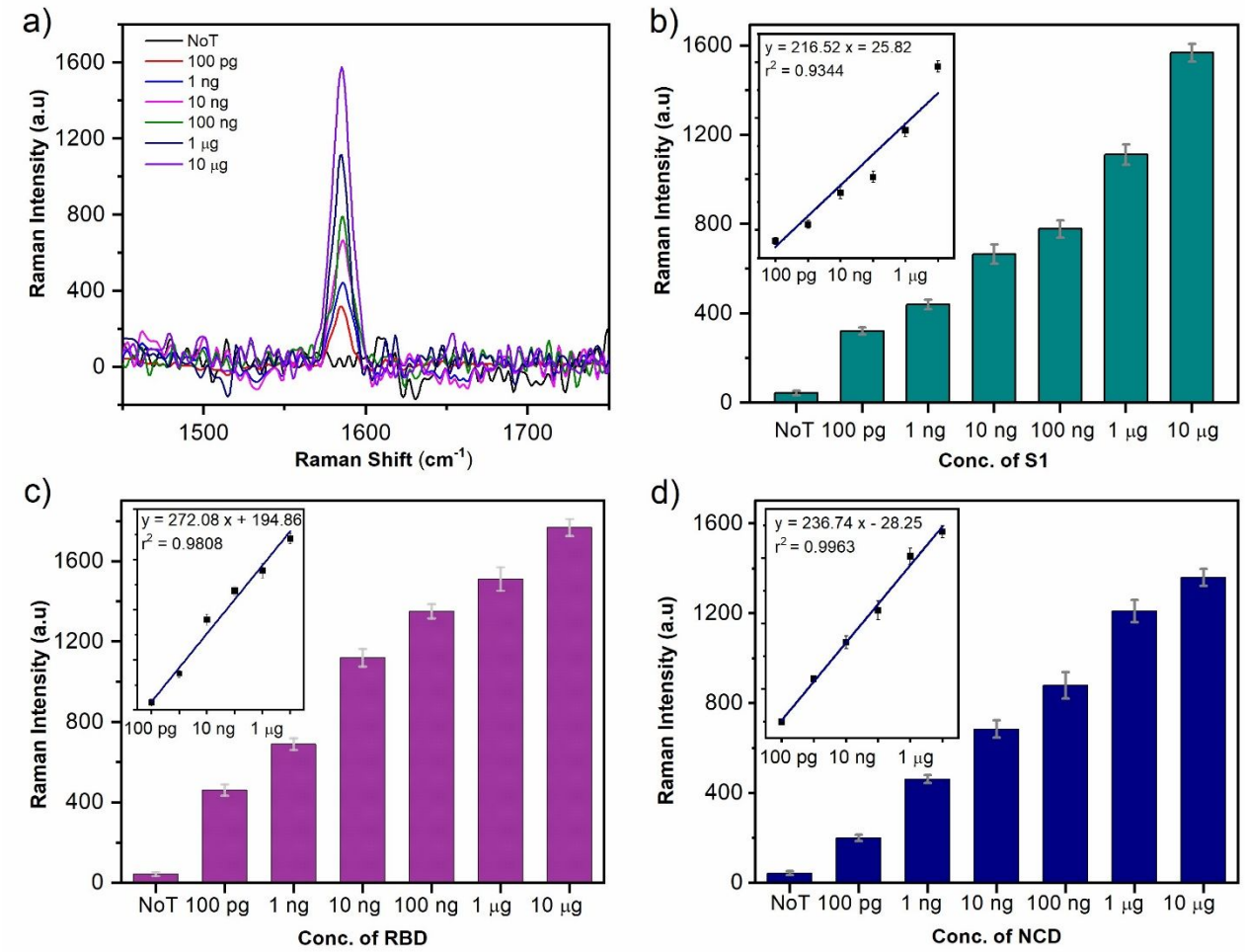

Figure 5. Platform sensitivity. (a) Raman spectra for S1 concentrations ranging from 10 µg/mL to 100 pg/mL. Extracted average Raman intensities for different concentrations based on the peak at 1585 cm^{-1} (b) of S1 protein; (c) RBD and (d) NCD proteins (*insets show the* corresponding linear regression curves.). Error bars indicate standard deviation (SD < 5.0) of replicates.

Our microfluidic biosensor offers numerous advantages: *i*) It integrates incubation, washing, and assay formation, enabling portability, reducing sample and reagent consumption, and facilitating point-of-care testing. *ii*) The use of plasmonic mAuNPs enables ultrasensitive detection with high loading of antibodies and SERS molecules. *iii*) All incubations and assay formations are performed at room temperature, allowing our device to be conducted on-site similar to RAT. *iv*) The PCR technique, while considered the gold standard, necessitates sophisticated laboratories and expert

operators. Commercial rapid kits usually detect only a single protein, whereas this platform can be used as an easy-to-use device to detect three proteins simultaneously. Our device can accommodate multiplexed assays by utilizing a three-chamber setup, with each chamber designated for a specific SARS-CoV-2 protein. This design enables the concurrent screening and quantification of these proteins in a single run, allowing for the simultaneous detection of multiple proteins (analytes) within a single sample. *v*) The microfluidic platform is disposable, ensuring contamination-free analysis. *vi*) This microfluidic device is not only limited for the detection of the SARS-CoV-2 protein but can also be employed for diverse detection, including other proteins, extracellular vesicles, and other cellular biomarkers by adjusting the antibody SERS reporter and device functionalization with relevant antibodies.

Conclusions

We have developed a novel microfluidic platform capable of simultaneously detecting three proteins (antigens) in a single run, ensuring precise and sensitive identification of SARS-CoV-2 proteins, specifically S1, RBD, and NCD. Key features of our platform include a user-friendly, single-run experimental setup of the microfluidic device, designed for simultaneous detection of at least three proteins, coupled with mAuNPs-based SERS nanotags, ensuring functionality and simplicity. Our microfluidic platform allows for the analysis of three proteins along with two controls in a single run using a minimal sample volume of approximately 100 μL. Furthermore, it can detect proteins at levels as low as 14 pg/mL, with a relative standard deviation (RSD) of less than 5.0% ($n = 3$). In comparison with existing approaches, our platform offers several crucial improvements for the analysis of SARS-CoV-2-like infectious diseases. Firstly, it provides a multiplex detection system along with controls. Secondly, it facilitates a simple experimental setup and a single-device-based complete assay platform. Thirdly, the use of mAuNPs-based SERS reporter eliminates the need for enzymatic amplification used in conventional assays. Finally, the portability of the SERS readout enhances its applicability for on-site detection and analysis, circumventing the necessity for intricate

instrumentation or laboratory settings. Given the inherent advantages of single-run, simultaneous detection, precision, on-the-spot analysis, and cost-efficiency, alongside the superior sensitivity and operational simplicity of our platform, we assert that this microfluidic system holds substantial promise for the development of a streamlined yet highly effective screening tool for infectious disease diagnosis, detection, and surveillance.

Experimental Section

Design and fabrication of the diagnostic devices. The polydimethylsiloxane (PDMS)-based microfluidic device was fabricated through a combination of soft lithography with a negative thick photoresist (SU-8 3050) and a wax reflow technique (**Figure S1**). The detailed fabrication procedures are outlined in the reference.[28] Figure S2 illustrates the microfluidic device employed in this research, featuring one inlet, six outlets, and five semielliptical microchambers (assay chambers) with a maximum depth of 1 mm. These assay chambers are interconnected via a rectangular microchannel measuring 51.4 μm in height and 196.3 μm in width. As depicted in **Figure S2**, each assay chamber is equipped with a pair of passive stop valves (S_1 and S_2) at the inlet and outlet, regulating burst pressure. This arrangement enables sequential dispensing of the analyte solution into the array of five assay chambers, each holding approximately 3 μL. The gap distances for valves S_1 and S_2 are meticulously set at 40.0 μm and 21.2 μm, respectively, resulting in burst pressures of P_1 = 1.87 kPa and P_2 = 4.97 kPa.[46] Following complete filling of all assay chambers with the sample solution, the common outlet port is sealed using adhesive double-sided tape. Subsequently, the chambers undergo washing with PBS buffer. Noteworthy is the adjustment of flow resistance, equivalent to the microchannel length, on the outlet side of each assay chamber. This adjustment ensures a consistent flow rate of liquid from the individual outlet ports of all chambers.

Functionalization on the glass surface with antibody. The PDMS microfluidic device was placed onto a glass to enable a 5-array detection platform. Before bonding with PDMS, the glass slide was

cleaned using an oxygen plasma cleaner for 10 minutes. The PDMS-glass assembly was heated to 90 ºC for 1 hour, and the platform was kept in the oven for an additional hour to strengthen the bonding effect. Subsequently, 2-(N-morpholino)ethanesulfonic acid was infused to prepare the surface of each chamber. To bind the IgG antibodies, the surface of was coated with a 1-ethyl-3-(3-dimethylaminopropyl)carbodiimide/N-hydroxysuccinimide (EDC/NHS) solution. Following this, the microfluidic device with EDC/NHS was incubated at 4 ºC for 20 hours. After three washes with binding and washing (b&w) buffer, 1 µg/mL of streptavidin was passed through each chamber and allowed to incubate overnight at 4 ºC. Finally, 200 ng/mL biotinylated antibodies (first two chambers with IgG, 3rd, 4th and 5th chambers with biotinylated anti-S1, RBD and NCD antibodies, respectively), were passed through each chamber and allowed to bind to the glass surface through biotin-streptavidin interactions.

Synthesis of mAuNPs. The mAuNPs were synthesized using a soft-templating strategy involving polystyrene-*b*-poly(ethylene oxide), following our established procedures.[31] At 40 °C, 1.25 mg of polystyrene-*b*-poly(ethylene oxide) ($PS_{18,000}$-*b*-$PEO_{7,500}$) was fully dissolved in 0.25 mL of tetrahydrofuran (THF). Sequentially, 125 µL of ethanol, 57 µL of 750 mM KOH, and 127 µL of 10 mM L-cysteine were added to the solution. The mixture was stirred gently for 20 minutes in an ice bath. Next, a cold solution of aqueous 80 mM $HAuCl_4$ (188 µL) was introduced to bind Au^{3+} ions to the micelles. Subsequently, 100 mM (250 µL) of ascorbic acid (AA) was added and stirred for 2 minutes. After this addition, the solution's colour transitioned from dark transparent yellow to colourless and eventually to reddish-blue as the final product was formed. The reaction mixture underwent an additional stirring for 1 h in an ice bath. The resulting product was collected by centrifugation at 14,000 rpm for 15 minutes and washed using THF/ethanol (1:1) before another round of centrifugation. This washing process was repeated eight times to remove the polymeric micelle template.

Preparation of mAuNPs-MBA SERS nanotags. By creating a mixed thiol monolayer composed of dithiobis succinimidyl propionate (DSP) and Raman reporters, we synthesized SERS tags and subsequently conjugated IgG antibodies. Briefly, to generate the mixed thiol monolayer, 2 µL of 1.0 mM DSP in dimethylsulfoxide (DMSO) and 100 µL of 4-MBA in ethanol (1 mM) were incubated for approximately 12 hours with 1 mL of mAuNPs under magnetic stirring. In the presence of DSP, the mAuNPs were combined with Raman reporters to create SERS nanoprobes. Raman reporters were linked to the mesoporous surface of AuNPs through the chemisorption of an aromatic thiol. The supernatants were extracted by centrifuging the colloid for 15 minutes at 6,500 rpm before being resuspended in 200 µL of PBS buffer. Following this, 200 µL of anti-IgG was added, and the colloid was incubated for 1 hour at an ambient temperature. The amine groups of the IgG bound to the succinimidyl ester of DSP, facilitating the conjugation. To remove unconjugated IgG, the colloid was centrifuged for 15 minutes at 6,500 rpm at 4 °C before being resuspended in 200 µL of 0.1% BSA (bovine serum albumin) for an additional 30 minutes at room temperature. BSA was introduced to the SERS nanoprobes as a stabilizing agent to prevent the aggregation of the SERS nanotags aggregation and minimize non-specific protein binding on the surface of the SERS nanotags.

Microfluidic platform for the detection of RBD, NCD and S1. A sandwich assay was formed on each chamber. The platform was designed to facilitate the analysis of three samples along with two controls. The first chamber served as a no-template control (NoT), where PBS was used instead of capture antibody. The second chamber acted as another control, where the nanotags were replaced with PBS. The remaining three chambers were dedicated to form assays with the target proteins. A mixture of three antigens (RBD, S1, and NCD) at a concentration of 10 ng/mL was delivered through the inlet using a syringe pump. After filling each chamber (except the first one) with the mixture sample, the platform was incubated for 30 minutes. Following incubation, the chambers were washed with the binding and washing (b&w) buffer. Subsequently, the target chambers (3^{rd}-5^{th}) were incubated with IgG-loaded mAuNPs nanotags. After a 30-minute incubation, each chamber was

washed with the b&w buffer to remove all unbound or loosely bound nanotags. A portable hand-held Raman spectrophotometer (MIRA; NA = 0.50, 1 mm and 7.6 mm working distance; 0.042–2.5 mm measuring spot size) was employed to obtain the SERS readout (at a wavelength of 785 nm) from each chamber for analysis.

Data analysis. The limit of detection (LOD) for the SERS microassay was established using the following equation: LOD = 3 × (SD of Raman signal of the noise) / (slope of the calibration curve), where SD denotes the standard deviation, and the noise was derived from the Raman signal intensity of the no template (NoT) control. To evaluate the experiment's reproducibility, the coefficient of variation (%CV) was computed using the formula: %CV = (SD/mean).

Conflicts of interest

There are no conflicts of interest to declare.

Acknowledgements

This study is supported by the Cancer Council Queensland Next Generation Cancer Research Fellowship to M.K.M (ID 202707). Y.Y. thanks the financial support from JST-ERATO Yamauchi Materials Space-Tectonics Project (JPMJER2003) and the UQ-Yonsei international project. Y.V.K. acknowledges the funding from the Queensland government through the Advance Queensland Fellowship Program (AQIRF043-2020-CV). Y.B and S.M.A. acknowledge the financial support provided by the Distinguished Scientist Fellowship Program (DSFP) of the King Saud University, Riyadh, Kingdom of Saudi Arabia. This work used the Queensland node of the NCRIS-enabled Australian National Fabrication Facility (ANFF). We express our gratitude to English editing software, such as Grammarly and ChatGPT, for checking grammatical errors in our manuscript, and to BioRender for creating Figure 1.

References

(1) R. E. Baker, A. S. Mahmud, I. F. Miller, M. Rajeev, F. Rasambainarivo, B. L. Rice, S. Takahashi, A. J. Tatem, C. E. Wagner, L. F. Wang, *Nat. Rev. Microbiol.,* 2022, **20**, 193-205.

(2) C. Buckee, A. Noor, L. Sattenspiel, *Nature,* 2021, **595**, 205-213.

(3) C. C. Lai, T. P. Shih, W. C. Ko, H. J. Tang, P. R. Hsueh, *Int. J. Antimicrob. Agents,* 2020, **55**, 105924.

(4) Q. Sun, H. Qiu, M. Huang, Y. Yang, *Ann. Intensive Care,* 2020, **10**, 1-4.

(5) S. L. Emery, D. D. Erdman, M. D. Bowen, B. R. Newton, J. M. Winchell, R. F. Meyer, S. Tong, B. T. Cook, B. P. Holloway, K. A. McCaustland, *Emerg. Infect. Dis.* 2004, **10**, 311.

(6) R. M. Amer, M. Samir, O. Gaber, N. A. El-Deeb, A. A. Abdelmoaty, A. A. Ahmed, W. Samy, A. H. Atta, M. Walaa, R. H. Anis, *J. Infect. Public Heal.,* 2021, **14**, 1446-1453.

(7) J. Bigio, E. L. MacLean, R. Das, G. Sulis, M. Kohli, S. Berhane, J. Dinnes, J. J. Deeks, L. E. Brümmer, C. M. Denkinger, *The Lancet Microbe,* 2023, **4**, 875-882.

(8) O. Puhach, B. Meyer, I. Eckerle, *Nat. Rev. Microbiol.,* 2023, **21**, 147-161.

(9) W. Yan, Y. Zheng, X. Zeng, B. He, W. Cheng, *Signal Transduct. Target. Ther.,* 2022, **7**, 26.

(10) R. Yadav, J. K. Chaudhary, N. Jain, P. K. Chaudhary, S. Khanra, P. Dhamija, A. Sharma, A. Kumar, S. Handu, *Cells,* 2021, **10**, 821.

(11) Y. Zhou, L. Zhang, Y. -H. Xie, J. Wu, *Lab. Invest.,* 2022, **102**, 4-13.

(12) A. D. Kaye, E. M. Cornett, K. C. Brondeel, Z. I. Lerner, H. E. Knight, A. Erwin, K. Charipova, K. L. Gress, I. Urits, R. D. Urman, *Best Pract. Res. Clin. Anaesthesiol.,* 2021, **35**, 269-292.

(13) E. A. Tarim, M. Anil Inevi, I. Ozkan, S. Kecili, E. Bilgi, M. S. Baslar, E. Ozcivici, C. Oksel Karakus, H. C. Tekin, *Biomed. Microdevices,* 2023, **25**, 10.

(14) P. Yager, T. Edwards, E. Fu, K. Helton, K. Nelson, M. R. Tam, B. H. Weigl, *Nature,* 2006, **442**, 412-418.

(15) Y. Yang, Y. Chen, H. Tang, N. Zong, X. Jiang, *Small Methods,* 2020, **4**, 1900451.

(16) J. Kneipp, H. Kneipp, K. Kneipp, *Chem. Soc. Rev.,* 2008, **37**, 1052-1060.

(17) K. B. Shanmugasundaram, J. Li, A. A. I. Sina, A. Wuethrich, M. Trau, *Mater. Adv.,* 2022, **3**, 1459-1471.

(18) G. Demirel, H. Usta, M. Yilmaz, M. Celik, H. A. Alidagi, F. Buyukserin, *J. Mater. Chem. C.,* 2018, **6**, 5314-5335.

(19) Y. Kang, M. K. Masud, Y. Guo, Y. Zhao, Z. S. Nishat, J. Zhao, B. Jiang, Y. Sugahara, T. Pejovic, T. Morgan, M.S.A. Hossain, H. Li, C. Salomon, T. Asahi, Y. Yamauchi, *ACS Nano,* 2023, **17**, 3346-3357.

(20) L. Liu, K. Pan, K. Xu, J. Z. Zhang, *ACS Phys. Chem. Au.,* 2022, **2**, 156-170.

(21) A. Chatterjee, P. Kar, *ACS Appl. Nano Mater.,* 2020, **3**, 2733-2744.

(22) G. Awiaz, J. Lin, A. Wu, *Exploration,* 2023, **3**, 20220072.

(23) Z. Wang, S. Zong, Y. Wang, N. Li, L. Li, J. Lu, Z. Wang, B. Chen, Y. Cui, *Nanoscale,* 2018, **10**, 9053-9062.

(24) S. Kaja, A. Nag, *Langmuir,* 2023, **39**, 16562-16573.

(25) E. Prodan, C. Radloff, N. J. Halas, P. A. Nordlander, *Science,* 2003, **302**, 419-422.

(26) K. M. Hastie, H. Li, D. Bedinger, S. L. Schendel, S. M. Dennison, K. Li, V. Rayaprolu, X. Yu, C. Mann, M. Zandonatti, D. Avalos, *Science,* 2021, **374**, 472-478.

(27) K. An, X. Zhu, J. Yan, P. Xu, L. Hu, C. Bai, *AIMS Microbiology,* 2022, **8**, 595.

(28) D. Natsuhara, R. Saito, H. Aonuma, T. Sakurai, S. Okamoto, M. Nagai, H. Kanuka, T. Shibata, *Lab. Chip.,* 2021, **21**, 4779-4790.

(29) S. Ding, L. Ma, J. Feng, Y. Chen, D. Yang, Q. Wang, *Nano Res.,* 2022, **15**, 2715-2721.

(30) X. Meng, L. Qiu, G. Xi, X. Wang, L. Guo, *SmartMat.,* 2021, **2**, 466-487.

(31) A. S. Nugraha, O. Guselnikova, J. Henzie, J. Na, M. S. A. Hossain, Ö. Dag, A. Rowan, Y. Yamauchi, *Chem. Mater.,* 2022, **34**, 7256-7270.

(32) C. Li, Ö. Dag, T. D. Dao, T. Nagao, Y. Sakamoto, T. Kimura, O. Terasaki, Y. Yamauchi, *Nat. Commun.,* 2015, **6**, 6608.

(33) B. D. Kevadiya, J. Machhi, J. Herskovitz, M. D. Oleynikov, W. R. Blomberg, N. Bajwa, D. Soni, S. Das, M. Hasan, M. Patel, *Nat. Mater.,* 2021, **20**, 593-605.

(34) K. Zhang, Z. Wang, H. Liu, N. Perea-López, J. C. Ranasinghe, G. Bepete, A. M. Minns, R. M. Rossi, S. E. Lindner, S. X. Huang, M. Terrones, *ACS Photonics,* 2022, **9**, 2963-2972.

(35) Z. Li, Y. Luo, Y. Song, Q. Zhu, T. Xu, X. Zhang, *Anal. Chim. Acta,* 2022, **1234**, 340523.

(36) M. Zhang, X. Li, J. Pan, Y. Zhang, L. Zhang, C. Wang, X. Yan, X. Liu, G. Lu, *Biosens. Bioelectron.* 2021, **190**, 113421.

(37) P. C. Guan, H. Zhang, Z. Y. Li, S. S. Xu, M. Sun, X. M. Tian, Z. Ma, J. S. Lin, M. M. Gu, H. Wen, F. L. Zhang, *Anal. Chem.,* 2022, **94**, 17795-17802.

(38) D. Antoine, M. Mohammadi, M. Vitt, J. Dickie, S. S. Jyoti, M. A. Tilbury, P. A. Johnson, K. E. Wawrousek, J. G. Wall, *ACS sensors,* 2022, **7**, 866-873.

(39) P. Liang, Q. Guo, T. Zhao, C. Y. Wen, Z. Tian, Y. Shang, J. Xing, Y. Jiang, J. Zeng, *Anal. Chem.,* 2022, **94**, 8466-8473.

(40) K. Daoudi, K. Ramachandran, H. Alawadhi, R. Boukherroub, E. Dogheche, M. A. El Khakani, M. Gaidi, *Surfaces and Interfaces,* 2021, **27**, 101454.

(41) Y. Xie, Q. Li, J. Chen, W. Yue, Z. Xia, M. Zeng, Y. He, Y. Zhao, X. Luo, *Sens. Actuators B Chem.,* 2023, **394**, 134470.

(42) Y. J. Yeh, T. N. Le, W. W. W. Hsiao, K. L. Tung, K. K. Ostrikov, W. H. Chiang, *Anal. Chim. Acta,* 2023, **1239**, 340651.

(43) J. Li, P. Liang, T. Zhao, G. Guo, J. Zhu, C. Wen, J. Zeng, *Anal. Bioanal. Chem.,* 2023**, 415**, 545-554.

(44) L. Fabiani, M. Saroglia, G. Galatà, R. De Santis, S. Fillo, V. Luca, G. Faggioni, N. D'amore, E. Regalbuto, P. Salvatori, G. Terova, *Biosens. Bioelectron.,* 2021, **171**, 112686.

(45) C. Vedelago, J. Li, K. Lowry, C. Howard, A. Wuethrich, M. Trau, *ACS Sensors,* 2023, **8**, 1648-1657.

(46) M. A. Abrar, Y. Dong, P. K. Lee, W. S. Kim, *Sci. Rep.,* 2016, **6**, 30565.

Footnote

† Electronic supplementary information (ESI) available. See DOI:... ... ...

The data supporting this article have been included as part of the Supplementary Information.